Journal of The Electrochemical Society, **153** (4) D74-D83 (2006)
0013-4651/2006/153(4)/D74/10/$20.00 © The Electrochemical Society

$La_{0.4}Sr_{0.6}Ti_{1-x}Mn_xO_{3-\delta}$ Perovskites as Anode Materials for Solid Oxide Fuel Cells

Q. X. Fu, F. Tietz,[z] and D. Stöver

Institute for Materials and Processes in Energy Systems, Forschungszentrum Jülich GmbH, 52425 Jülich, Germany

Perovskite oxides, $La_{0.4}Sr_{0.6}Ti_{1-x}Mn_xO_{3-\delta}$ (x = 0, 0.2, 0.4, 0.6), have been investigated in the search for new solid oxide fuel cell (SOFC) anode materials. $La_{0.4}Sr_{0.6}Ti_{0.4}Mn_{0.6}O_{3-\delta}$ (LSTM4646) shows an electrical conductivity of 22.6 S/cm in air and 1.5 S/cm in wet Ar/4% H_2 [$p(O_2) \approx 10^{-18}$ bar] at 810°C. It is thermally and chemically compatible with yttria-stabilized zirconia (YSZ) electrolytes. Three processes govern the electrochemical performance of LSTM4646/YSZ anodes in wet Ar/H_2 or wet CH_4. They are proposed to be charge transfer at the LSTM4646/YSZ interface, dissociative adsorption of hydrogen on the electrode surface, and gas conversion impedance, respectively. Due to the low polarization resistance of the LSTM4646/YSZ anode, 0.32 Ω cm^2, an electrolyte-supported H_2/air fuel cell with an LSM/YSZ cathode yields a power density of 365 mW cm^{-2} at 0.7 V at 856°C. In addition, this anode material is stable under a moderately humidified hydrogen atmosphere. It shows insignificant catalytic activity for the direct oxidation of methane however.
 [DOI: 10.1149/1.2170585]

Manuscript submitted November 21, 2005; revised manuscript received December 12, 2005.
Available electronically February 24, 2006.

One of the most attractive features of solid oxide fuel cells (SOFCs) is that they can use hydrocarbon fuels (e.g., natural gas) directly to generate electrical energy in a highly efficient way. Carbon monoxide, which is inevitable in the reforming products of hydrocarbons, is rather a fuel than a poison as is the case in proton exchange membrane fuel cells (PEMFCs). To realize this feature, an efficient anode is of particular importance. Currently, corresponding to the most promising electrolyte material, yttria-stablized zirconia (YSZ), the most widely used anode material, is a Ni/YSZ cermet. This composite anode works well with internal steam-reformed methane, showing excellent catalytic activity as well as good current collection. However, it also has many disadvantages, including nickel coarsening, sulfur poisoning, carbon deposition, and volume instability upon cyclic reduction–oxidation (redox). In addition, nickel and nickel oxide are materials that may cause cancer or allergies, posing difficulties in handling and processing of these materials. Therefore, it would be advantageous to develop alternative anode materials to overcome problems with Ni/YSZ.

From the viewpoint of volume stability upon redox cycling, an all-ceramic anode is preferable because the oxidation/reduction of metals like Ni or Cu is always accompanied by a large volume change. In recent years, many ceramic oxides with various crystal structures, such as rutile, fluorite, perovskite, pyrochlore, and tungsten bronze, have been investigated as anode materials.[1-14] Among them, the perovskite oxides, mainly titanates and chromites, which are chemically stable under anode conditions, have been studied more intensively. For instance, La-substituted $SrTiO_3$ materials show high electrical conductivity in reducing atmosphere as well as good dimensional and chemical stability upon redox cycling, but the electrocatalytic activity for H_2 oxidation is very poor.[2] Further modification of these materials with CeO_2 greatly improved the electrocatalytic activity for H_2 oxidation.[3] However, it is actually a two-phase composite containing $(Ce,La)O_{2-\delta}$ and $(Sr,La)TiO_{3-\delta}$, in which the catalytic activity is provided by the ceria phase. It is thus not surprising that this composite material still shows insufficient electrocatalytic activity for CH_4 oxidation,[3] because doped ceria itself is not a good catalyst for CH_4 oxidation.[4,5] The application of ceria-containing anode on YSZ-based SOFCs may also be limited by the detrimental reaction between ceria and YSZ at elevated temperatures forming a poorly conductive intermediate layer,[15] especially when a co-firing step of the anode/electrolyte bilayer is required. Y-substituted $SrTiO_3$ also shows high electrical conductivity, but so far no good fuel cell performance has been reported with this material.[6,7]

Due to their good stability and high electrical conductivity, it is also anticipated that $LaCrO_3$-based interconnect materials[16] can be modified to anode materials through appropriate elemental substitution. Therefore, various transition metal elements (e.g., Ru, V, Mn, Fe, Co, Ni) with 3–10 atom % concentration were inserted into the Cr site of the perovskite lattice, and the Ni substitution seemed most promising.[8-11] However, further investigations revealed nickel segregation from the perovskite lattice upon reduction,[12] Thus, the observed good electrocatalytic activity of 10 atom % Ni-substituted $(La,Sr)CrO_3$ could be ascribed to the well-dispersed metallic Ni because the catalytic effect of only a small fraction of Ni in an anode has been demonstrated by other investigations.[17-19] Recently, a high-level Mn-substituted lanthanum strontium chromite, $La_{0.75}Sr_{0.25}Cr_{0.5}Mn_{0.5}O_{3-\delta}$ (LSCM), was reported to display rather good electrochemical performance.[13,14] The electrode polarization resistance at 900°C was 0.26 and 0.87 Ω cm^2 in wet H_2 and wet CH_4, respectively. The observed good performance of this material could be linked to its possibly improved ionic conductivity by the 50 atom % Mn substitution for Cr because the ionic conductivity was found to be crucial for a mixed ionic/electronic conductor to have good electrocatalytic activity for fuel oxidation.[1] In reducing atmosphere and at high temperatures, the reduction of Mn leads to an oxygen loss of as much as 0.25 mol O^{2-} per mol of LSCM,[14] giving rise to a high concentration of oxygen vacancies. The strong ability of oxygen incorporation/release of LSCM upon redox cycling is essentially due to the presence of 50 atom % Mn, which is capable of adjusting its valence (+4, +3, and +2) according to the ambient oxygen partial pressure ($p(O_2)$), as in $(La,Sr)MnO_3$.[20-22]

As stated above, despite its high electronic conductivity, La-substituted $SrTiO_3$ itself has little electrocatalytic activity for fuel oxidation. It is possible, however, to improve its activity through a high level of Mn substitution on the Ti site. Due to the good chemical stability of $(La,Sr)TiO_3$ perovskites in reducing atmosphere, Mn is expected to be stabilized in the perovskite lattice in a way similar to that in LSCM. In this work, $La_{0.4}Sr_{0.6}Ti_{1-x}Mn_xO_{3-\delta}$ (x = 0, 0.2, 0.4, 0.6) perovskites were synthesized and evaluated as potential anode materials in terms of crystal structure, chemical stability, thermal and chemical expansion, as well as electrical and electrochemical properties.

Experimental

Powder synthesis.— The Pechini method[23] was used to synthesize the powders with the following compositions:

[z] E-mail: f.tietz@fz-juelich.de

$(La_{0.4}Sr_{0.6})TiO_{3-\delta}$ (LST), $La_{0.4}Sr_{0.6}Ti_{0.8}Mn_{0.2}O_{3-\delta}$ (LSTM4682), $La_{0.4}Sr_{0.6}Ti_{0.6}Mn_{0.4}O_{3-\delta}$ (LSTM4664), and $La_{0.4}Sr_{0.6}Ti_{0.4}Mn_{0.6}O_{3-\delta}$ (LSTM4646). The Mn-containing compositions are generally designated as LSTM throughout this paper. Nitrates of La, Sr, Mn, and titanium isopropoxide were used as the starting chemicals. To control the final compositions as precisely as possible, the hygroscopic nitrates were first dissolved in water and then assayed by the thermogravimetric method. Titanium isopropoxide was dissolved in ethylene glycol and citric acid to form a stable solution that can be mixed with other nitrate aqueous solutions without causing precipitation. The Ti content in the as-prepared Ti solution was also assayed by the thermogravimetric method. During the concentrating process of the precursor solution, no precipitate or turbidity was observed, indicating the near-molecular-level cation mixing through the whole process. The resulting resins were then calcined at 900°C for 5 h to completely burn out the organic substances and to form the expected crystalline phases. The as-prepared powders may be used directly for the preparation of electrode pastes or subjected to further calcination at higher temperatures to achieve better crystallization, e.g., for structural stability studies.

Characterization.— Powder X-ray diffraction (XRD) with Cu Kα radiation (Siemens D5000) was used to characterize the phase purity of air-sintered samples as well as those subjected to various subsequent heat-treatments in reducing atmospheres. The XRD patterns were analyzed with related softwares including PowderX[24] and Dicvol91.[25] The structural stability to reduction was studied by exposing the air-calcined (at 1300°C) powders at different $p(O_2)$ and temperatures and examining the resulting phases by XRD. To study the reactivity with YSZ, LSTM powders were mixed with commercial YSZ powder (Tosoh, TZ-8Y) in a 1:1 weight ratio and then calcined at 1400°C for 5 h in air.

Powders were uniaxially pressed into bars and then sintered in air. LSTM samples were densified to over 95% of theoretical density by sintering in air at 1300°C for 5 h. However, the LST sample was difficult to sinter, with only 70% theoretical density achieved under the same sintering conditions. The as-obtained rectangular-shaped samples with dimensions of 3 × 4 × 40 cm were subjected directly to electrical conductivity measurements, or cut to a length of 25 mm before dilatometric measurements. As the electrical conductivity of LST was found to be very sensitive to the sintering atmosphere,[2] one LST sample was prereduced at 1320°C for 20 h in Ar/4% H_2 before the electrical conductivity measurements. The thermal expansion measurements (25–1100°C in air) and chemical expansion upon redox cycling were carried out using a push-rod dilatometer (Netzsch DIL 402C) with heating and cooling rates of 3 K/min. The standard dc four-probe method was used to measure the electrical conductivity in air and reducing atmosphere (wet Ar/4% H_2) at 100–910°C. Unless specified, gas humidification was performed by passing the gases through a water container at ambient temperatures (20–28°C). A zirconia oxygen sensor (Metrotec) was used to monitor the $p(O_2)$ at 700°C, and the $p(O_2)$ at other temperatures was then deduced by thermodynamic calculations of the H_2–O_2–H_2O system.

The electrode polarization resistances were characterized by electrochemical impedance spectroscopy (EIS) with a symmetric cell configuration. TZ-8Y powder was first pressed into pellets and then sintered at 1500°C for 10 h to obtain dense YSZ electrolyte substrates (Ø 12 mm and 1–2 mm thick). LSTM or LSTM/YSZ composite electrodes were applied onto both surfaces of the YSZ substrates by screen printing and then calcined in air at 1200°C for 3 h. A content of 35 vol % YSZ in the composite electrodes was chosen in order to supply an additional percolating ionic transport path while retaining as much as possible the electronic conduction path provided by the LSTM phase. Furthermore, the YSZ in the composite electrode was added to improve the adhesion to the electrolyte. The thickness and diameter of the electrodes are 15–30 μm and 10 mm, respectively. Before the EIS measurements, Au paste (Ferro, 64101003) was applied onto the electrodes by screen printing and then calcined at 800°C for 1 h to obtain a current collection layer with a thickness of 3–5 μm. The impedance spectra of the electrochemical cells were obtained with a Solartron 1260 frequency response analyzer working in a galvanostatic mode. The ac current amplitude was 3 mA and the frequency range was 10^6–0.05 Hz. The reducing atmosphere used in this measurement is wet Ar/H_2 or wet CH_4 with a normal flow rate of 100 mL/min. The impedance spectra were analyzed with Zview software (Scribner Associates, Inc.). The microstructure of the electrodes was investigated by scanning electron microscopy (SEM, Zeiss Ultra55).

Fuel cell performance with LSTM/YSZ anodes was also measured in wet H_2 or wet CH_4 vs air. YSZ sheets (Ø 20 mm and 0.2 mm thick, Kerafol GmbH) were used as the electrolyte supports. Anodes were applied by screen printing and calcined in air at 1200°C for 3 h, then the LSM ($La_{0.65}Sr_{0.3}MnO_3$)-based double-layer cathodes [LSM–YSZ (1:1 wt %)/LSM] were applied by the same method and calcined in air at 1100°C for 3 h. Finally, Au current collectors were applied onto both sides in the same way as for the symmetric cells. The diameter of both electrodes was 12 mm. The gas flow rate of H_2, CH_4, or air was controlled at 200 mL/min. The humidification of the fuel gases was also performed at room temperature. Both the I-V curves and impedance spectra of the two-electrode asymmetric cells were measured at 750–860°C.

Results and Discussion

Crystal structure and electrical conductivity.— As determined by XRD, all four compositions show single-phase perovskite-type structures after sintering in air at 1300°C for 5 h. While LST exhib-

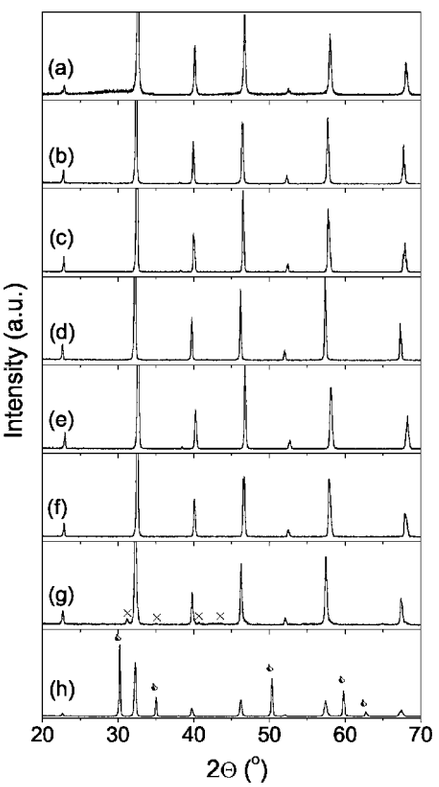

Figure 1. XRD patterns of $La_{0.4}Sr_{0.6}Ti_{1-x}Mn_xO_{3-\delta}$ samples subjected to different firing conditions: (a) LST, 1300°C for 5 h in air; (b) LST, 1150°C for 10 h in air, then 1320°C for 20 h in Ar/4% H_2; (c) LSTM4664, 1300°C for 5 h in air; (d) LSTM4664, 1300°C for 5 h in air, then 850°C for 12 h in Ar/4% H_2; (e) LSTM4646, 1300°C for 5 h in air; (f) LSTM4646, 1300°C for 5 h in air, then 950°C for 12 h in wet Ar/4% H_2; (g) LSTM4646, 1300°C for 5 h in air, then 850°C for 12 h in Ar/4% H_2 ("×" indicates impurities due to decomposition); and (h) LSTM4646/YSZ mixture, cosintered in air at 1400°C for 5 h (▽: YSZ).

Table I. Unit cell parameters of $La_{0.4}Sr_{0.6}Ti_{1-x}Mn_xO_{3-\delta}$ subjected to different firing conditions.

Composition	Firing conditions	Lattice setting	Lattice parameters
LST	1300°C/5 h/air	Cubic	a = 3.892(1) Å, V = 58.93(4) Å^3, Z = 1
LST	1150°C/10 h/air, then 1320°C/20 h/ Ar/4%H_2	Tetragonal	a = 7.811(3) Å, c = 2.964(1) Å, V = 180.9(2) Å^3, Z = 3
LSTM4682	1300°C/5 h/air	Hexagonal	a = 5.522(2) Å, c = 13.48(2) Å, V = 356.0(8) Å^3, Z = 6
LSTM4682	1300°C/5 h/air, then 950°C/12 h/ wet Ar/4%H_2	Hexagonal	a = 5.559(1) Å, c = 13.57(1) Å, V = 363.3(4) Å^3, Z = 6
LSTM4664	1300°C/5 h/air	Hexagonal	a = 5.528(1) Å, c = 13.483(4) Å, V = 356.8(2) Å^3, Z = 6
LSTM4664	1300°C/5 h/air, then 950°C/12 h/ wet Ar/4%H_2	Hexagonal	a = 5.540(2) Å, c = 13.505(6) Å, V = 359.0(4) Å^3, Z = 6
LSTM4646	1300°C/5 h/air	Hexagonal	a = 5.497(2) Å, c = 13.40(2) Å, V = 350.7(8) Å^3, Z = 6
LSTM4646	1300°C/5 h/air, then 950°C/12 h/ wet Ar/4%H_2	Tetragonal	a = 3.9015(6) Å, c = 15.552(4) Å, V = 236.7(1) Å^3, Z = 4

its cubic structure, the structures of LSTM can be best refined as hexagonal perovskites. Because LST is stable in highly reducing atmospheres,[2] only LSTMs were subjected to reduction under selected conditions to study the structural stability to reduction. After reduction in wet Ar/4% H_2 at 950°C ($p(O_2) \approx 2.3 \times 10^{-16}$ bar) for 12 h, all three compositions retained their perovskite structure. However, after reduction in nonhumidified Ar/4% H_2 at 850°C ($p(O_2) \approx 10^{-23}$ bar) for 12 h, the perovskite structures of LSTM4682 and LSTM4664 were still retained, whereas a slight decomposition of LSTM4646 was observed (Fig. 1). The decomposition products were identified as MnO and $(La,Sr)_2MnO_4$ with K_2NiF_4-type structure, both being previously reported as the decomposition products of $(La,Sr)MnO_3$.[26,27] The practical $p(O_2)$ in an SOFC anode chamber depends on the fuel cell working conditions, e.g., the inlet fuel composition, fuel utilization, anode polarization. The anode materials experience the lowest $p(O_2)$ when the fuel cell is under open-circuit conditions. In practice, humidification is usually carried out before H_2 or CH_4 is fed into the anode chamber to obtain a well-defined open circuit voltage (OCV) and to avoid extremely low $p(O_2)$. The present results indicate that LSTM4646 can only be used in a moderately humidified atmosphere. It seems stable at 800°C in an atmosphere with a H_2O/H_2 ratio of 3:20, as shown later.

The calculated lattice parameters of LST and LSTM in the oxidized as well as reduced state are listed in Table I. For comparison, the pseudo-cubic lattice parameters are plotted in Fig. 2. The reduced state of LST was obtained by a high-temperature (1320°C) reduction process in Ar/4% H_2, while LSTMs were only reduced at 950°C in wet Ar/4% H_2 to assure the phase integrity. These reduction conditions were chosen because LST shows strongly improved electrical conductivity after a high-temperature reduction process.[2] In this work, such a process leads to a lowered crystal symmetry refined as tetragonal for LST. In addition, it seems that LSTM4646 also changes its structure from hexagonal to tetragonal after reduction. Under oxidizing conditions, substitution of Mn for Ti leads to a gradual lattice expansion until x = 0.4, and further substitution to 60 atom % causes an apparent lattice shrinkage. Upon reduction, while all compositions show lattice expansions, the linear expansion of LSTM4664 (0.20%) is significantly smaller than that of LSTM4682 (0.69%) and LSTM4646 (0.39%).

The electrical conductivity in both air and humidified Ar/4% H_2 of air-sintered $La_{0.4}Sr_{0.6}Ti_{1-x}Mn_xO_{3-\delta}$ as a function of temperature and Mn content is shown in Fig. 3 and 4. For a better comparison, the electrical conductivity data were corrected with the sample density according to an empirical equation proposed by Tagawa et al.[28]

$$\sigma_{app}/\sigma_{corr} = 2(d_{rel}/100 - 0.5) \quad [1]$$

where σ_{corr} is the corrected electrical conductivity, σ_{app} the measured apparent conductivity, and d_{rel} the relative density (%).

In oxidizing atmosphere, the electrical conductivity increases monotonically with Mn content. However, the behavior in reducing atmosphere is quite different. In fact, both the electrical property and the crystal structure can be linked to the inherent charge compensa-

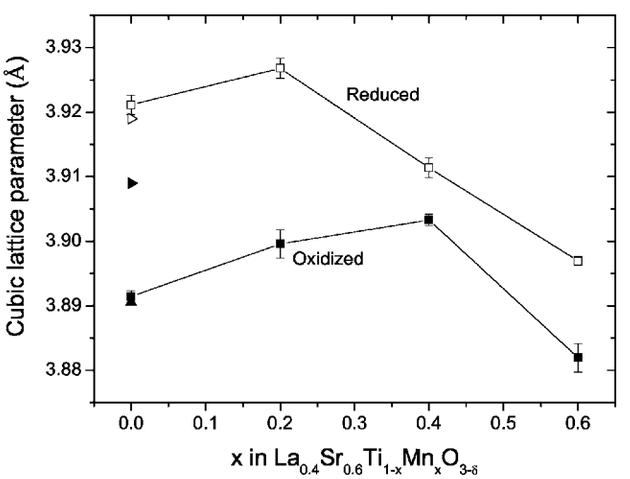

Figure 2. Pseudo-cubic lattice parameters of $La_{0.4}Sr_{0.6}Ti_{1-x}Mn_xO_{3-\delta}$ as a function of Mn content in both oxidized (closed symbols) and reduced (open symbols) states. The pseudo-cubic lattice parameter is defined as the cubic root of the primitive cell volume, i.e., $a = \sqrt[3]{V/Z}$. Squares are results of this work. Detailed firing conditions and calculated lattice parameters are listed in Table I. Even the structure of oxidized LST is not really cubic due to the appearance of the diffusive "background" (see the text). Triangles are results from the literature for LST. (▶): Annealed at 1400°C for 17 h in air;[41] (▷): annealed at 1400°C for 17 h in N_2/10% H_2;[41] (▲) annealed at 1350°C in air (note: the parameter remains unchanged after reduction at 1050°C in CO/CO_2).[38]

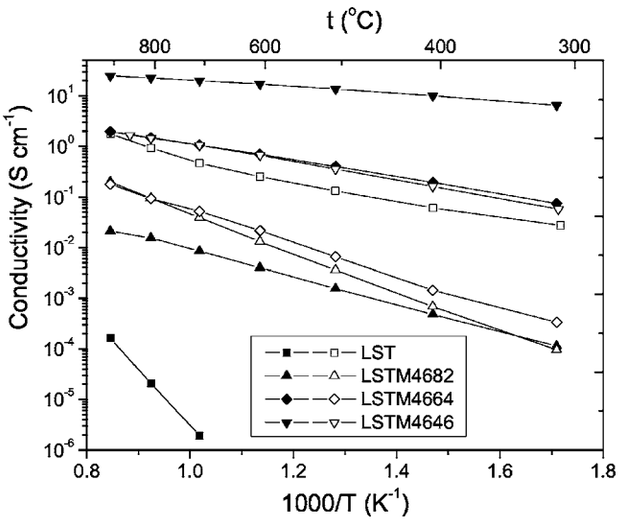

Figure 3. Temperature dependence of the electrical conductivity of $La_{0.4}Sr_{0.6}Ti_{1-x}Mn_xO_{3-\delta}$ (x = 0,0.2,0.4,0.6) materials sintered in air and measured in both air (closed symbols) and wet Ar/4% H_2 (open symbols).

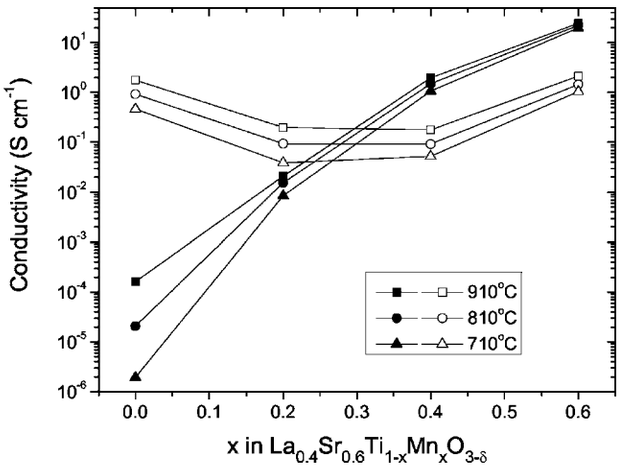

Figure 4. Electrical conductivity of $La_{0.4}Sr_{0.6}Ti_{1-x}Mn_xO_{3-\delta}$ as a function of Mn content at 710, 810, and 910°C in both air (closed symbols) and humidified Ar/4% H_2 (open symbols).

tion mechanisms, which vary with the atmosphere (or $p(O_2)$) and the Mn content in $La_{0.4}Sr_{0.6}Ti_{1-x}Mn_xO_{3-\delta}$. This is discussed from the viewpoint of defect chemistry.

For the Mn-free composition, LST, the replacement of Sr^{2+} by La^{3+} requires charge compensation to ensure charge neutrality in the lattice. In moderately reducing atmospheres, e.g., water-saturated Ar/H_2, the formation of oxygen vacancies can be neglected. The charge compensation is then realized by the reduction of Ti^{4+} to Ti^{3+}, i.e., $[La_{Sr}^{\cdot}] = [Ti_{Ti}']$ using Kröger–Vink[29] notation. Thus, the composition may be represented by $(La_{Sr}^{\cdot})_{0.4}(Sr_{Sr}^{\times})_{0.6}(Ti_{Ti}')_{0.4}(Ti_{Ti}^{\times})_{0.6}(O_O^{\times})_3$. This compensation mechanism has been demonstrated by Moos et al.[30-32] who determined Ti^{3+} concentration by various methods (chemical titration, thermopower, and Hall measurements). Under extremely reducing conditions, oxygen vacancies are formed, giving rise to more Ti^{3+} according to $[La_{Sr}^{\cdot}] + 2[V_O^{\cdot\cdot}] = [Ti_{Ti}']$. In atmospheres with high $p(O_2)$, however, Ti^{3+} is unlikely to exist in the material; thus, the charge neutrality dictates the presence of additional oxygen beyond the ABO_3 stoichiometry ($La_{0.4}Sr_{0.6}TiO_{3.2}$). One way to accommodate the extra oxygen is the formation of A-site cation vacancies coupled with planar defects similar to those in the Ruddlesden–Popper phases ($Sr_{n+1}Ti_nO_{3n+1}$),[33,34] where SrO layers are interleaved within perovskite layers. Assuming this compensation mechanism, the composition LST may be represented by $(La_{Sr}^{\cdot})_{0.4}(V_{Sr}'')_{0.2}(Sr_{Sr}^{\times})_{0.4}Ti_{Ti}^{\times}O_3 \cdot (SrO)_{0.2}$. This model seems very reasonable due to (*i*) the existence of a perovskite (ABO_3) phase of the A-site deficient composition $Sr_{1-1.5x}La_xTiO_3$,[35,36] where Sr vacancies compensate the positive charge from $La_{Sr}^{\cdot}$, and (*ii*) the ability of Ruddlesden–Popper phases to accommodate SrO layers structurally in an ordered manner.[33,34,37] Therefore, wide agreement on this issue was reached in the literature,[2,38-41] although no strong direct evidence was reported.

With the help of high-resolution transmission electron microscopy (HRTEM), Bowden et al.[42] and later Canales-Vázquez et al.[43] showed that the extra oxygen in La-substituted $SrTiO_3$ is actually accommodated by the creation of planar defects similar to those of $La_2Ti_2O_7$.[44] No cation vacancy is required in this mechanism. Thus, La-substituted $SrTiO_3$ ($Sr_{1-x}La_xTiO_{3+0.5x}$) can be described as a structural solid solution of $La_2Ti_2O_7$-type layers in $SrTiO_3$. This solution occurs across the entire $Sr_{1-x}La_xTiO_{3+0.5x}$ composition range ($0 \leqslant x \leqslant 1$). At higher levels of substitution ($x \geqslant 0.67$), such layers are ordered into new compounds, which are clearly visible by HRTEM and also detectable by diffraction methods. These compounds are represented by the general formula $La_4Sr_{n-4}Ti_nO_{3n+2}$, and the members with n = 4.5, 5, 6 have been investigated in detail by Bowden et al.[42] and Canales-Vázquez et al.[43] With lower levels of substitution, the concentration of $La_2Ti_2O_7$-type layers becomes smaller and they are randomly distributed throughout the perovskite host. XRD patterns may only show a broadened perovskite signal.

The lanthanum content of $x = 0.4$ is equivalent to the member with $n = 10$ of $La_4Sr_{n-4}Ti_nO_{3n+2}$. With this composition, Bowden et al.[42] found the $La_2Ti_2O_7$-type layers either in clusters or in isolation, and accordingly, some weak impurity peaks in the XRD pattern. Although in our present work the XRD diffraction pattern of LST sintered in air can be fitted with a cubic symmetry, a diffusive "background" that is significantly higher than in other samples is also clearly visible (Fig. 1a). It is considered that higher annealing temperatures or longer annealing times would lead to better ordering of those $La_2Ti_2O_7$-type layers, and hence, transform the "background" to sharp impurity peaks, as observed previously.[42,43] In their work, Bowden et al. annealed the sample at 1350°C for 16 h, and Canales-Vázquez et al. did this at 1400–1600°C for 96 h. In comparison, the LST sample in this work was only sintered at 1300°C for 5 h.

In summary, under oxidizing conditions, the substitution of La^{3+} for Sr^{2+} in $SrTiO_3$ does not lead to electronic (via Ti_{Ti}') or ionic (via V_{Sr}'') compensation but only to excess oxygen accommodated by $La_2Ti_2O_7$-type layers in the structure. Due to the excess of oxygen in this material, oxygen vacancies are unlikely to exist. The lack of both electronic charge carrier (Ti_{Ti}') and ionic charge carrier ($V_O^{\cdot\cdot}$) results in very low electrical conductivity (cf. Fig. 3). Upon reduction, the excess oxygen in LST can be removed, as confirmed by thermogravimetric experiments,[38,40,43] transferring LST to a reduced state. The concentration of electronic charge carriers (Ti_{Ti}') is then significantly increased, resulting in a jump of electrical conductivity by at least 4 orders of magnitude (Fig. 3 and 4). Higher reduction temperatures or longer reduction times would remove more excess oxygen and create a higher concentration of Ti_{Ti}'. In the present work, reduction of air-sintered LST at 910°C for 15 h in humidified Ar/4% H_2 only yields a conductivity of 1.8 S/cm at 910°C, whereas the sample annealed in Ar/4% H_2 at 1320°C for 20 h shows a conductivity of 50 S/cm under the same experimental conditions (not shown in Fig. 3 and 4). Similar results were reported by Marina et al.[2] As discussed above, the removal of excess oxygen tends to integrate the $La_2Ti_2O_7$-type layers into the structure, which is con-

sistent with the disappearance of such a diffusive "background" in the XRD pattern of a highly reduced LST sample (Fig. 1b).

The lattice parameter of the highly reduced LST (3.921(2) Å) observed here is consistent with the results obtained by Howard et al.[41] (3.919 Å, Fig. 2). However, for the oxidized LST, the obtained lattice parameter (3.891(1) Å) is much smaller than Howard's (3.909 Å). Instead, it is very close to the results of Eror and Balachandran[38] (3.8905 Å). Nevertheless, Eror and Balachandran[38] found no significant change of lattice parameter when the oxidized LST was reduced. This is consistent with the results in Ref. 43, where only a slightly smaller lattice parameter was observed when the material $La_{0.33}Sr_{0.67}TiO_{3+\delta}$ was reduced (3.9065(4) vs 3.9094(4) Å). These discrepancies could be ascribed to the different annealing conditions used by the authors. With respect to the oxidized states, Howard et al.[41] and Canales-Vázquez et al.[43] annealed their samples at 1400–1600°C for 17–48 h in air. In contrast, the present authors and Eror and Balachandran[38,45] performed this annealing under relatively moderate conditions, 1300–1350°C for 5–10 h in air, which might cause incomplete ordering and smaller lattice parameters. With respect to the reduced states, samples were reduced either at 1000–1050°C[38,43] or at 1320–1400°C (this work and Ref. 41). Canales-Vázquez et al.[43] showed that reduction of $La_{0.33}Sr_{0.67}TiO_{3+\delta}$ at 1000°C for 48 h in Ar/H_2 produced only 8–10 atom % Ti^{3+} (the fully reduced state should have 33 atom % Ti^{3+}). Eror and Balachandran[38] also pointed out that the redox kinetics at 1050°C became very slow when the La^{3+} concentration exceeded 20 atom %. In comparison, full reduction/oxidation of 20 atom % La-substituted $SrTiO_3$ was realized at 1300°C within a reasonable period of time.[40] Therefore, it can be concluded that a fully reduced state of LST might have been achieved in Ref. 41 and in our work, which in turn led to significantly increased lattice parameters.

The replacement of LST by Mn at the B-site supplies an additional compensation mechanism. While the replacement of Sr^{2+} by La^{3+} would lead to excess oxygen in the structure under oxidizing conditions, the replacement of Ti^{4+} by Mn^{3+} would have a counter-effect, presumably leading to fewer $La_2Ti_2O_7$-type layers in the structure. This effect, together with the difference in ionic radius between Mn and Ti, may lead to the observed gradual increase of the lattice parameters with Mn content up to 40 atom %. At a Mn content of 40 atom %, i.e., for LSTM4664, complete neutralization (between $La_{Sr}^{\cdot}$ and Mn_{Ti}') is expected, and excess oxygen is then not required anymore. In this sense, LSTM4664 might be simply regarded as a solid solution of $LaMnO_3$ and $SrTiO_3$, i.e., $(LaMnO_3)_{0.4}(SrTiO_3)_{0.6}$. Further substitution of Mn either creates oxygen vacancies or increases the valence of Mn itself. Due to the smaller ionic radius of Mn^{4+}, the latter might result in a smaller lattice parameter, as shown in Fig. 2.

Upon reduction, both Mn and Ti tend to have lower valence states and larger ionic radii, giving rise to larger lattice parameters. It is not surprising that the fully "neutralized" composition, LSTM4664, shows significantly smaller lattice expansion upon reduction compared with its two neighboring compositions, LSTM4682 and LSTM4646. Compared with LSTM4664, LSTM4682 might contain much more excess oxygen that is readily removable and thus would show a larger lattice expansion upon reduction. For LSTM4646, if we assume a Mn^{4+} compensation mechanism under oxidizing conditions, i.e., $(La_{Sr}^{\cdot})_{0.4}(Sr_{Sr}^{\times})_{0.6}(Ti_{Ti}^{\times})_{0.4}(Mn_{Ti}')_{0.4}(Mn_{Ti}^{\times})_{0.2}(O_O^{\times})_3$, the existence of a significant amount of Mn^{4+} ($Mn_{Ti}^{\times}$) facilitates the reduction of this compound, also resulting in more oxygen release upon reduction than LSTM4664. This can be better understood when we consider the oxygen nonstoichiometry of $(La,Sr)MnO_3$. Compared with $LaMnO_3$, in which the average valence of Mn is +3, $La_{0.8}Sr_{0.2}MnO_3$ requires 20 atom % Mn^{4+} for charge compensation. $La_{0.8}Sr_{0.2}MnO_3$ shows much higher oxygen substoichiometry after reduction.[20,22] It is thus envisaged that the reduced LSTM4646 might contain a significant amount of oxygen vacancies, which gives rise to a remarkably improved ionic conductivity and therefore good electrocatalytic activity for fuel oxidation.

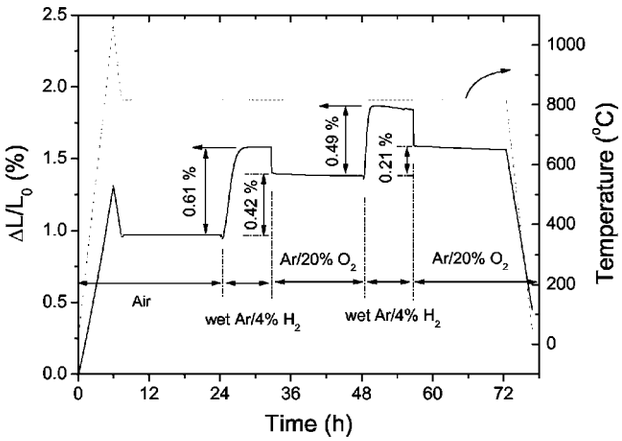

Figure 5. Thermal and chemical expansion behavior of a dense LSTM4646 sample. The sample is heated to 1060°C in air to obtain the thermal expansion coefficient. After cooling in air to 817°C, the sample is then subjected to two redox cycles between wet Ar/4% H_2 and Ar/20% O_2 to observe the chemical expansion.

$SrTiO_3$ or La-substituted $SrTiO_3$ is known as an n-type semiconducting material, in which the electrical conductivity increases with decreasing $p(O_2)$.[39,46] The electrical conductivity is essentially controlled by the concentration of the electronic defect, Ti^{3+} or Ti_{Ti}'. Instead, $LaMnO_3$ or Sr-substituted $LaMnO_3$ is a p-type conductor, and its electronic conductivity is determined by the mean Mn valence.[22] It should be noted that even the stoichiometric $LaMnO_3$ exhibits a fairly high electrical conductivity in air (~80 S/cm at 800°C), although the mean Mn valence is +3. After reduction, the electronic conductivity of $(La,Sr)MnO_3$ is decreased due to the lowered mean Mn valence, but its oxide ionic conductivity is increased due to the significantly increased oxygen vacancy concentration.[21] Under oxidizing conditions, the electrical conductivity of LSTM increases monotonically with Mn content and is remarkably higher than that of LST (Fig. 4). Therefore, it can be concluded that the electrical conductivity of LSTM in the oxidizing atmosphere is dominated by the p-type conduction related to Mn. In reducing atmosphere, however, the n-type conductivity related to Ti^{3+} is greatly improved, whereas the p-type conductivity related to Mn is decreased. The reduced LSTM4682 shows lower conductivity than the reduced LST but higher conductivity than the oxidized LSTM4682, indicating that the n-type electrical conductivity still predominates in the reduced LSTM4682. It seems that 20 atom % Mn substitution partially offsets the n-type contribution from Ti^{3+}. Due to this shift, the electrical conductivity of the reduced LSTM4664 is one order of magnitude lower than its oxidized state. When the Mn concentration exceeds the La concentration, p-type conduction predominates, leading to a significantly improved electrical conductivity for the reduced LSTM4646.

The electrical conductivity of LSTM4646 reached 1.5 S/cm at 810°C in wet Ar/4% H_2, which might be acceptable for a thin anode functional layer. Assuming the electrical conductivity of a porous LSTM4646/YSZ electrode is 1 order of magnitude lower than the dense LSTM4646 material (which is a good estimate according to Ref. 47), an anode functional layer 15-μm-thick would give rise to an area-specific resistance of about 0.01 Ω cm^2 at 800°C. Due to the rather low electrical conductivity of the other compositions in reducing atmosphere, only LSTM4646 was subjected to further dilatometric measurement and electrochemical performance characterization.

Regarding the reactivity of LSTM4646 with YSZ, the room tem-

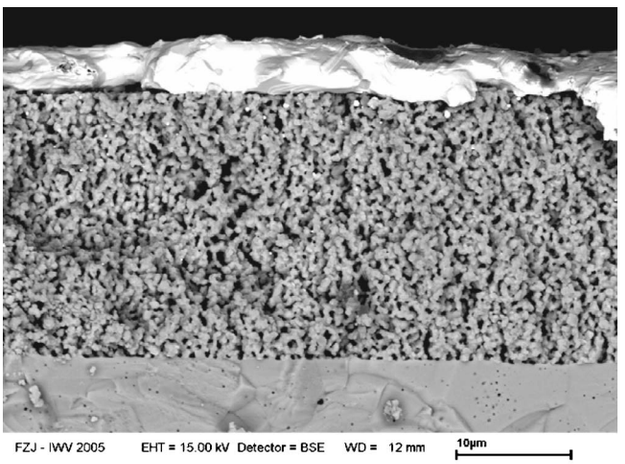

Figure 6. SEM picture of the LSTM4646/YSZ anode on YSZ electrolyte. Top layer is Au current collector.

perature XRD patterns of cofired LSTM4646/YSZ powders (Fig. 1h) show no apparent impurity phase, indicating good chemical compatibility of LSTM4646 with YSZ up to at least 1400°C.

Thermal and chemical expansion.— The thermal and chemical expansion behavior of a dense LSTM4646 sample is shown in Fig. 5. The average thermal expansion coefficient (30–1000°C in air) is 11.9×10^{-6} K^{-1}, which is close to that of YSZ ($10.6–10.9 \times 10^{-6}$ K^{-1}[148]). However, a chemical expansion of as much as 0.61% is observed when the material is reduced in wet Ar/4% H_2 at 817°C. As discussed above, the room-temperature XRD results show a chemical expansion of 0.39% between the oxidized and reduced state of LSTM4646. The larger chemical expansion observed by dilatometric measurement at 817°C could be ascribed to either a higher thermal expansion coefficient of the reduced LSTM4646 than that of the oxidized LSTM4646, or the appearance of microcracks in the sample during the high-temperature reduction process. The subsequent reoxidation process in Ar/20% O_2 cannot fully restore the sample to its original size, leaving an irreversible expansion of 0.42%, definitely indicating the existence of microcracks in the sample. Judging from the shape of the expansion curve, the reoxidation process is much faster than the reduction process. The expansion curve at the reduction stage shows a typical diffusion-limited behavior, corresponding to the oxygen bulk diffusion in the dense LSTM material. This may indicate that microcracks are not formed during the reduction process. Instead, this occurs at the beginning of the reoxidation process, leading to fast oxidation kinetics because oxygen can be easily transported through the microcracks to the interior of the sample. The second redox cycle causes an additional irreversible expansion of 0.21%, indicating that more microcracks were formed.

Considering a chemical expansion of 0.5% during redox cycling, this corresponds to a lateral dimensional change of 0.5 mm, or even 1 mm for a 10×10 cm^2- or a 20×20 cm^2-sized SOFC. Such large changes may induce strong stresses on the adjacent components, especially on the electrolyte layer in an anode-supported cell. Whereas an electrolyte-supported cell might have enough strength due to the thicker electrolyte layer, the stresses during redox cycling may lead to cracks in the electrolyte of an anode-supported cell. To evaluate more precisely the applicability of LSTM in different types of SOFCs, thermomechanical calculations have to be carried out. On the basis of the results so far, an application of LSTM can only be recommended for electrolyte-supported cells and/or small-sized SOFCs like the integrated planar-type SOFC,[49] in which the dimensions of the cells are kept small in comparison to typical anode-supported cells.[50]

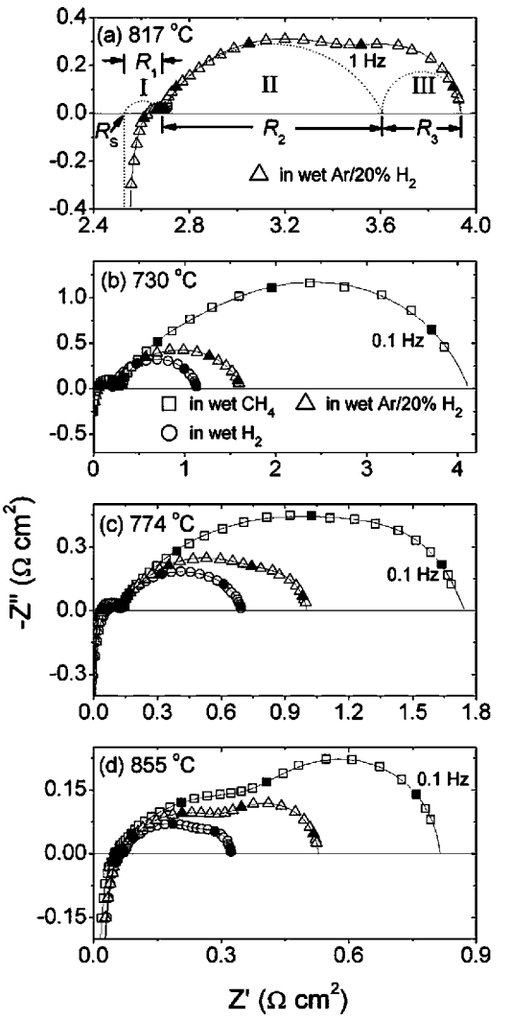

Figure 7. Selected impedance spectra of one LSTM4646/YSZ electrode on YSZ electrolyte at different temperatures in wet CH_4 (squares), wet Ar/20% H_2 (triangles), and wet H_2 (circles). Points are experimental data and solid lines are fit data with the equivalent circuit $LR_S(RQ)_1(RQ)_2(RQ)_3$. In (a) dotted lines indicate each impedance arc in the fit of one set of as-obtained impedance data of one symmetric cell, which is only corrected for the active electrode area. In (b)–(d) the series resistances R_S are subtracted and the resulting spectra are then divided by 2 to directly give the polarization resistances (R_p) of one electrode. Closed symbols mark the frequency points from 0.1 Hz to 100 kHz at each frequency decade.

Electrochemical performance and long-term stability.— The electrodes under study show uniform porous structures and good adhesion to the YSZ electrolytes (Fig. 6). In the impedance spectra of the symmetric cells in wet Ar/H_2 or wet CH_4, three arcs are generally observed in the frequency range of 10^6–0.05 Hz. Only in a few cases are two arcs visible due to the overlap of two adjacent arcs. Examples of the impedance spectra of LSTM4646/YSZ anodes obtained at different temperatures and in different atmospheres are shown in Fig. 7. In general, data are fitted to the equivalent circuit $LR_S(RQ)_1(RQ)_2(RQ)_3$, following the circuit description codes used elsewhere.[51] This simple equivalent circuit is chosen on the basis of no prior knowledge of the limiting reactions or any evidence supporting a more refined analysis. The inductance L is primarily ascribed to the leads, and a typical value is 1.5×10^{-7} H for the present measurement system. The series resistance of the symmetric cell, R_S, is mainly ascribed to the electrolyte resistance due to the relatively thick electrolyte substrates (1–2 mm) used. This is con-

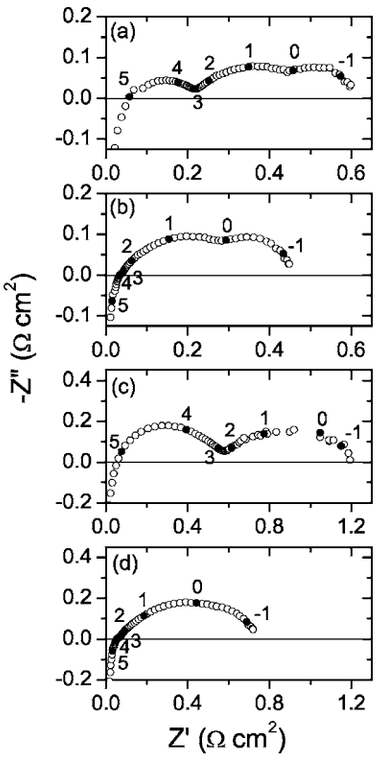

Figure 8. Comparison of the impedance spectra between LSTM4646 and LSTM4646/YSZ anodes in wet H_2 at two temperatures: (a) LSTM, 810°C; (b) LSTM/YSZ, 810°C; (c) LSTM, 760°C; and (d) LSTM/YSZ, 760°C. The original impedance spectra obtained with the symmetric cells were processed in the same way as in Fig. 7b-d to show directly the polarization resistances (R_p) of one electrode. Closed symbols as well as numbers beside them indicate the frequency decades (0.1 Hz–100 kHz).

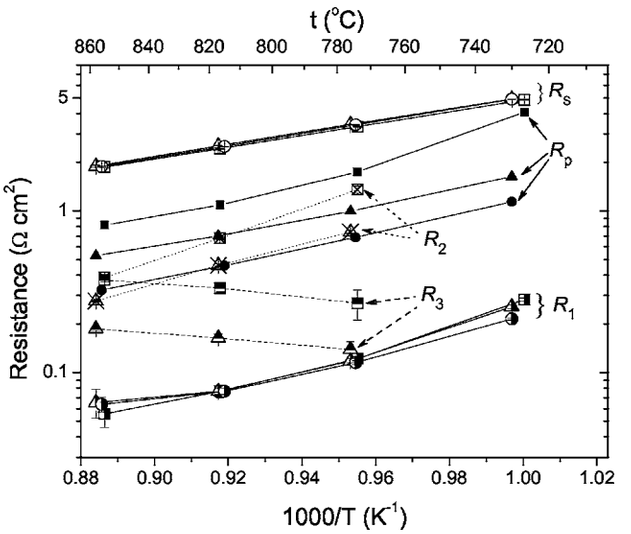

Figure 9. Temperature dependence of R_S, R_1, R_2, R_3, and R_p ($=R_1 + R_2 + R_3$) of one symmetric cell with LSTM4646/YSZ electrodes in wet CH_4 (squares), wet Ar/20% H_2 (triangles), and wet H_2 (circles). The electrode polarization resistances (R_1, R_2, R_3, and R_p) were divided by 2 to give the contribution of one single electrode. In cases where arc 2 and arc 3 overlapped too extensively to be distinguished with good certainty, separate R_2 and R_3 values are not shown on the graph.

firmed by the comparison of the fitted R_S values with the real electrolyte resistance calculated from the known ionic conductivity of the electrolyte material and the cell geometry. In all cases, they are very close to each other. Figure 7a gives an example of detailed fitting, where three well-distinguished arcs are shown and numbered I, II, and III from high to low frequency.

For each arc represented by a parallel RQ, the fitted resistance, R, admittance, Y_0, and frequency power, n, are used to calculate the summit frequency of the arc, f_{max}, according to Eq. 2.[52] The capacitance $C(f)$ at any given frequency f of a (RQ) subcircuit is calculated according to Eq. 3[52]

$$f_{max} = \frac{1}{2\pi}(RY_0)^{-1/n} \quad [2]$$

$$C(f) = Y_0(2\pi f)^{n-1}\sin\left(\frac{n\pi}{2}\right) \quad [3]$$

Each parallel RQ corresponds physically to one of the processes occurring in the complex electrode reactions. The fitted parameters (R, Y_0, n) and derived parameters [e.g., f_{max}, $C(f_{max})$] for each arc help to identify the corresponding process. Under the present experimental conditions, the summit frequency of the high-frequency arc, arc I, is generally over 10 kHz, which is distinctively higher than the low-frequency arcs (1–20 Hz for arc II and 0.2–2 Hz for arc III). Due to such high summit frequencies, part of this arc is often "dragged" down by the inductance to below the real axis on the complex impedance plane ($-Z''$ vs Z'), as shown in Fig. 7a. In the cases where arc II and III overlap extensively, attempts to fit them with only one (RQ) subcircuit, however, often lead to much worse fitting results. Therefore, all the impedance data are fitted to the circuit $LR_S(RQ)_1(RQ)_2(RQ)_3$, although, in some cases, the fitted parameters for arc II and III contain large uncertainties and hence are not shown in the related graphs. The polarization resistance of the electrode, R_p, is defined as $R_1 + R_2 + R_3$.

Under the same experimental conditions, LSTM4646 anodes show larger polarization resistances than LSTM4646/YSZ anodes. As shown in Fig. 8, the main difference of the impedance spectra between LSTM4646 and LSTM4646/YSZ anodes lies in arc I (with peak frequency around 30 kHz). LSTM4646 anodes show a remark-

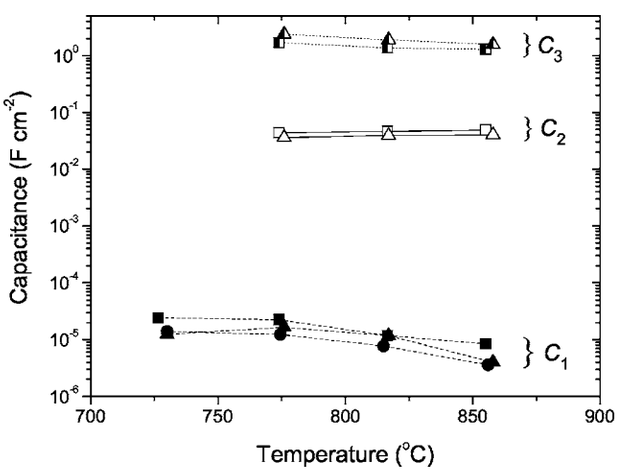

Figure 10. Calculated capacitances at the summit frequency of arc I (C_1), arc II (C_2), and arc III (C_3) for each impedance spectra measured. Calculations were performed according to Eq. 2 and 3 in combination with the fitting results (R, Y_0, n) for the impedance spectra measured at different temperatures and in wet CH_4 (squares), wet Ar/20% H_2 (triangles), and wet H_2 (circles).

ably enlarged arc I, while having almost the same sized arc II and III as LSTM4646/YSZ anodes. This difference helps to determine the nature of process I, as discussed below.

The fitted results of resistances and capacitances (at the summit frequency) for the impedance spectra of LSTM4646/YSZ anodes under various experimental conditions are shown in Fig. 9 and 10. As expected, R_S is only a function of temperature and does not vary with the atmosphere. The activation energy for R_S is calculated as 0.83 ± 0.02 eV, which is consistent with that of the ionic transport in YSZ in the high-temperature region (0.85 ± 0.05 eV), as reported in the literature.[53]The dependence of the three arcs on the experimental conditions, e.g., temperature, atmosphere composition, and gas flow rate, are summarized as follows:

1. Arc I remains essentially unchanged when the atmosphere is changed from wet Ar/20% H_2 to wet H_2 or to wet CH_4. In contrast, both arc II and arc III vary with the hydrogen content in wet Ar/H_2 and show larger sizes in wet CH_4 than in wet Ar/20% H_2 (Fig. 7, 9, and 11).
2. The gas flow rate of Ar/H_2 has no apparent effect on the overall impedance spectra, as shown in Fig. 11.
3. Process I and II are apparently thermally activated, but process III is slightly thermally deactivated (Fig. 9). The apparent thermal activation energy for process I is roughly determined as 0.9–1.5 eV due to the large fitting uncertainty as the size of arc I is significantly reduced at higher temperatures. The activation energy for process II is 1.7 and 1.3 eV in wet CH_4 and wet Ar/20% H_2, respectively. Process III has an apparent thermal activation energy of about -0.2 eV in both wet CH_4 and wet Ar/20% H_2.
4. The capacitances for all three processes are essentially independent of the temperature and atmosphere composition. C_1, C_2, and C_3 are in the ranges of 5–20 μF cm^{-2}, 30–50 mF cm^{-2}, and 1.5–2.5 F cm^{-2}, respectively (Fig. 10).

The capacitance of process I is in the same order of magnitude as a typical double-layer capacitance, i.e., ~ 10 μF cm^{-2}.[54,55] In addition, process I is thermally activated and is insensitive to the atmosphere composition. Therefore, arc I can be interpreted as a charge-transfer process taking place at the LSTM4646/YSZ interface. In studies of the hydrogen oxidation reaction on a Ni/YSZ anode, a high-frequency arc was observed[52] with similar characteristics, as can be seen here for arc I, and attributed to the transfer of charged species across the Ni/YSZ interface. In the present study, the fact that LSTM4646/YSZ anodes show a remarkably smaller arc I than LSTM4646 anodes strongly supports this interpretation. In the composite anode, the area of the LSTM4646/YSZ interface is effectively increased, leading to decreased charge-transfer resistance. This might also indicate that the ionic conductivity of the LSTM4646 phase is lower than that of YSZ.

Process II is also thermally activated and has a capacitance of 30–50 mF cm^{-2}. As calculated previously,[52] adsorption of a mono-charged species on a Ni/YSZ electrode surface would give a capacitance in the order of 10 mF cm^{-2}. By combining its sensitivity to the hydrogen concentration in wet Ar/H_2, this process is proposed to be linked to the dissociative adsorption of hydrogen on the electrode surface.

The capacitance of process III is larger than 1 F cm^{-2}. A capacitance of this magnitude is not ascribable to interfacial capacitance or adsorption on surfaces. Instead, a bulk process is required. So far two bulk processes have been reported to be able to give such a large capacitance. One is related to the chemical composition change of the electrode material under the effect of an applied potential. This capacitance is called a "chemical capacitance," which is generally observed in mixed conductors as described by Jamnik and Maier.[56,57]The chemical capacitance is proportional to the electrode volume. For a $La_{0.6}Sr_{0.4}CoO_{3-\delta}$ electrode a few micrometers thick, depending on the oxygen partial pressure and the temperature, a capacitance of 0.01–1 F cm^{-2} was observed.[58,59] The large capacitance originates from the change of oxygen nonstoichiometry in $La_{0.6}Sr_{0.4}CoO_{3-\delta}$ when the electrode potential is varied. In the present work, LSTM is also considered as a mixed conductor under the anode conditions, and the oxygen incorporation/release reaction at the electrode would also give rise to a large chemical capacitance. Under this assumption, the corresponding resistance should then be related to the oxygen exchange reaction on the electrode surface and/or oxygen bulk diffusion in the electrode, both of which are thermally activated. However, this would be in contradiction to the negative apparent thermal activation energy for process III. Therefore, chemical capacitance does not seem to be a good explanation for the large capacitance observed.

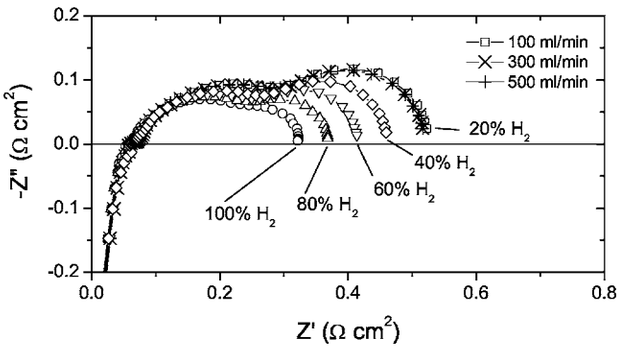

Figure 11. Influence of the gas flow rate (for wet Ar/20% H_2) and the hydrogen concentration in wet Ar/H_2 (at 100 mL/min) on the polarization resistance of one LSTM4646/YSZ electrode at 858°C. The gas was humidified at room temperature.

Another process that gives such large capacitance is called gas conversion.[60] The large capacitance of this process observed by impedance spectroscopy is related to the gas composition change in the vicinity of the electrode when a current is passed onto the electrode, leading to a variation in the Nernst potential. A low-frequency arc with a capacitance of up to several F cm^{-2} was observed in the impedance spectra of a Ni/YSZ electrode in wet H_2 at 1000°C in a three-electrode setup.[60]One important feature of this process is that the associated resistance would be slightly thermally deactivated (e.g., $E_a \approx -0.09$ eV, as calculated and observed in Ref. 52 and 60), which is consistent with the small negative apparent thermal activation energy (-0.2 ± 0.1 eV) observed in this work. However, gas conversion impedance should not be detectable in a small symmetric two-electrode cell where the electrodes are placed sufficiently close together in a common atmosphere. This is evidenced by the absence of such gas conversion impedance when the same Ni/YSZ electrode material was measured in a symmetric two-electrode cell setup (electrode area 0.25 cm^2, electrolyte thickness ~ 200 μm).[60] Furthermore, gas conversion impedance can be considerably depressed with a larger gas flow rate, whereas such a behavior is not observed here. However, the small negative apparent activation energy of process III strongly supports an explanation based on the gas conversion impedance, in opposition to the chemical capacitance.

According to its origin, the appearance of gas conversion impedance depends significantly on the experimental conditions like cell/setup geometry or gas flow profile. Even in a symmetric two-electrode cell, gas conversion impedance can be avoided only when the electrodes are so close together that any gas composition variation at one electrode can be followed simultaneously at the other electrode, giving rise to a zero Nernst potential change between these two electrodes. In this work, the cell (electrode area ~ 0.8 cm^2 and electrolyte thickness ~ 2 mm) is much larger than that used in Ref. 60. Therefore, it is possible that the requirement for the avoidance of gas conversion impedance as stated above is not fulfilled in the current cell under the experimental conditions applied so that gas conversion impedance is still present. As the temperature is lowered, R_3 is slightly decreased while R_2 is significantly increased due to the high activation energy of process II (1.3–1.7 eV); hence, arc III

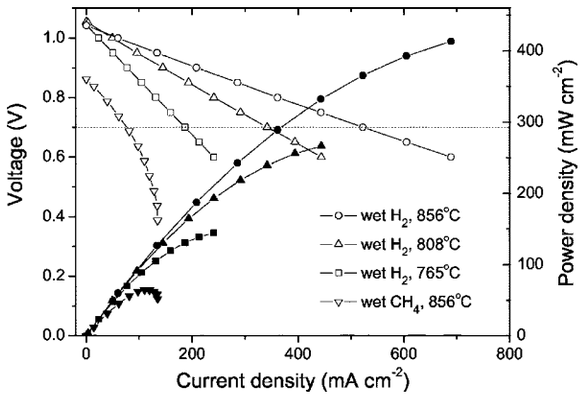

Figure 12. Electrochemical performance of a single fuel cell operated with wet H_2 or wet CH_4 as fuel gas and air as oxidant at different temperatures. The cell is electrolyte (213-μm-thick YSZ) supported, with LSTM4646/YSZ anode and LSM-based cathode.

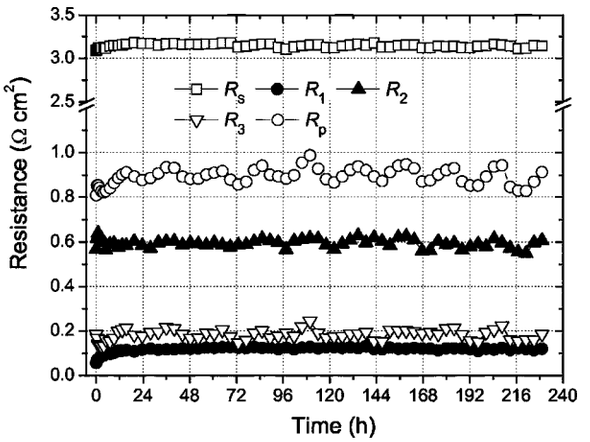

Figure 14. Time dependence of R_S, R_1, R_2, R_3, and R_p of one symmetric cell with LSTM4646/YSZ electrodes in wet Ar/20% H_2 at 795°C. Ar/20% H_2 was humidified at room temperature (20–28°C). The electrode polarization resistances (R_1, R_2, R_3, and R_p) were divided by 2 to give the contribution of one single electrode.

becomes less distinct and may be fully masked by the large arc II. This trend is clearly observed, as shown in Fig. 7. Nevertheless, further work is needed to determine with certainty the real process associated with arc III.

The total polarization resistance (R_p) of one LSTM4646/YSZ electrode as a function of temperature and atmosphere composition is also shown in Fig. 9. In wet H_2, R_p is 0.32 Ω cm^2 and 0.46 Ω cm^2 at 856 and 815°C, respectively. According to the apparent activation energy (1.07 ± 0.05 eV), R_p is estimated by extrapolation to be 0.22 Ω cm^2 in wet H_2 at 900°C. In wet CH_4, it increases to 0.82 and 1.09 Ω cm^2 at 855 and 816°C, respectively. In comparison, the polarization resistances of LSCM/YSZ anodes (optimized by grading) at 900°C were reported to be 0.51 Ω cm^2 in wet Ar/5% H_2, 0.26 Ω cm^2 in wet H_2, and 0.87 Ω cm^2 in wet CH_4.[19] Therefore, the electrochemical performance of LSTM4646/YSZ anode seems slightly better than that of LSCM/YSZ anode.

The performance of a fuel cell with LSTM4646/YSZ anode and LSM-based cathode is shown in Fig. 12. Wet CH_4 or H_2 is used as the fuel, and air is used as the oxidant. To separate the electrode polarization resistance from the total cell resistance, impedance spectra under open-circuit conditions corresponding to each I-V curve in Fig. 12 are measured and shown in Fig. 13. In wet H_2 and at 856°C, the OCV is very close to the theoretical electromotive force (1.05 vs 1.09 V), and a power density of 365 mW cm^{-2} at a terminal voltage of 0.7 V is observed. The peak powder density is not measured but can be estimated by extrapolation as 425 mW cm^{-2}. From the slope of the nearly linear I-V curve, the total cell resistance at this temperature is determined as 0.65 Ω cm^2, which is consistent with the low-frequency intercept on the corresponding impedance spectrum (0.68 Ω cm^2). From the impedance result, this total cell resistance is composed of an ohmic resistance of 0.32 Ω cm^2 and an electrode polarization resistance of 0.36 Ω cm^2. Here the electrode polarization resistance also includes the contribution from the cathode. As described above, the symmetric cell impedance measurement under the same conditions yields an R_p of 0.32 Ω cm^2, which agrees very well with the two-chamber asymmetric cell measurement.

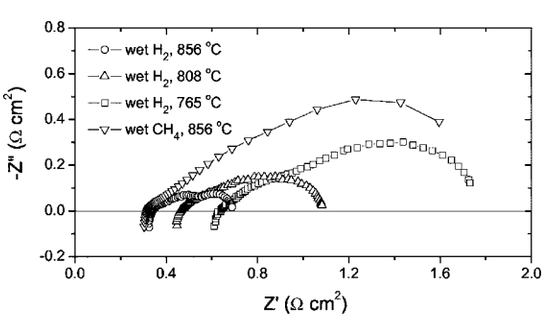

Figure 13. Impedance spectra under open-circuit conditions of the fuel cell corresponding to Fig. 11. Both anode and cathode contribute to the impedance spectra.

The fuel cell performance in wet CH_4, however, is much poorer than in wet H_2. The OCV at 856°C is only 0.86 V, and a limiting current density is observed. According to the symmetric cell measurement, the polarization behavior of LSTM4646/YSZ anodes in wet CH_4 looks very similar to that in wet Ar/H_2 (Fig. 7, 9, and 10). The polarization resistance in wet CH_4 is much larger than that in Ar/20% H_2. Considering the increased R_p with decreased H_2 content in wet Ar/H_2, the polarization of LSTM4646/YSZ electrode in wet CH_4 behaves in exactly the same way as in a more diluted H_2. In combination with the low OCV and limiting current observed with a fuel cell, it is thought that the LSTM4646/YSZ electrode does not have significant electrocatalytic activity for the direct oxidation of CH_4. Instead, the power output of the fuel cell in wet CH_4 can be primarily attributed to the oxidation of a small fraction of H_2 at the anode, which might be produced by steam reforming. After operation in wet CH_4 (~3% H_2O) for 2 h, the fuel cell performance recovers immediately and returns completely to its initial level when the gas is switched back to wet H_2, indicating that no significant carbon deposition occurred on the electrode during operation in wet CH_4. In fact, this is in accordance with the observed low OCV in wet CH_4, because a good cracking catalyst would lead to a high H_2 concentration and hence a high OCV, at least temporarily.

While this material shows good electrochemical performance for the oxidation of H_2, its long-term stability under typical anode conditions remains another major concern. To examine this, a symmetric cell was exposed to wet Ar/20% H_2 at 795°C for more than 200 h, and the polarization resistance was checked periodically by impedance measurements. The result is shown in Fig. 14. The first point on the graph was measured soon after the atmosphere was switched from air to wet Ar/20% H_2. During the first few hours, R_1 increased significantly, accompanied by a slight increase of R_S. This could be due to the reduction of the LSTM phase to a reduced state, with lowered electronic conductivity leading to an inhibition of the charge transfer process. At this stage, the lattice expansion of the LSTM phase upon reduction (Fig. 5) could also result in slight deterioration of the electrode microstructure. The connectivity between

LSTM and YSZ might thus be affected, also leading to an increased charge-transfer resistance. After this stage, R_1 and R_S remain nearly stable with time. Neglecting the periodic fluctuations, R_2, R_3, and R_p can be regarded as stable during the measurement time. Careful examination discloses that the periodic fluctuations have a period of 24 h. Therefore, this is likely caused by the day and night room temperature fluctuations (20–28°C), giving rise to a water content fluctuation in Ar/20% H_2 because the gas is simply humidified at ambient temperature. Compared to R_2, the relative fluctuation of R_3 seems larger (note its small absolute values). Therefore process III is more sensitive to the water content than process II. It is found that higher water content corresponds to smaller R_p. This would lead to better anode performance when a real fuel cell is operated at high fuel utilization, generating a high concentration of water in the anode chamber.

Conclusions

Perovskite oxides, $La_{0.4}Sr_{0.6}Ti_{1-x}Mn_xO_{3-\delta}$ (x = 0, 0.2, 0.4, 0.6), were synthesized and evaluated in detail as new anode materials for SOFCs. The charge compensation mechanism as a function of oxygen partial pressure and Mn content is considered to play a key role in determining the crystal structure as well as the electrical property. Among the compositions studied, $La_{0.4}Sr_{0.6}Ti_{0.4}Mn_{0.6}O_{3-\delta}$ (LSTM4646) shows an electrical conductivity of 1.5 S/cm at 810°C and $p(O_2)$ of $\sim 10^{-18}$ bar. In addition, it is thermally and chemically compatible with YSZ electrolytes.

Three processes govern the electrochemical performance of LSTM4646 or LSTM4646/YSZ electrodes in wet Ar/H_2 or wet CH_4. The two high-frequency processes are proposed to be charge transfer at the LSTM4646/YSZ interface and dissociative adsorption of hydrogen on the electrode surface. The third process corresponds to a very large capacitance (1.5–2.5 F cm^{-2}) and is slightly thermally deactivated. It is thus tentatively ascribed to gas conversion impedance.

LSTM4646/YSZ composite anodes show better electrochemical performance than LSTM4646 anodes. The polarization resistance is as low as 0.32 Ω cm^2 in wet H_2 at 856°C; therefore, an electrolyte-supported H_2/air fuel cell with an LSM/YSZ cathode yields a power density of 365 mW cm^{-2} at a terminal voltage of 0.7 V. In addition, it is stable in a moderately humidified hydrogen atmosphere. However, this anode shows insignificant electrocatalytic activity for the direct oxidation of methane. The chemical expansion of dense LSTM4646 material between air and wet Ar/4% H_2 is as much as 0.6% at 817°C and is not reversible. This property would restrict the application of this material for electrolyte-supported cells and/or small-sized SOFCs like the integrated planar-type SOFC.

Acknowledgments

This research was supported by a Marie Curie International Fellowship under contract no. MIF1-CT-2004-509999 within the Sixth European Community Framework Program. The authors thank Dr. D. Sebold (FZJ-IWV 1) for the SEM investigations, P. Lersch (FZJ-IWV 2) for the XRD measurements, and H. Wesemeyer and Dr. I. C. Vinke (FZJ-IWV 3) for assistance with the electrochemical characterization.

Forschungszentrum Juelich assisted in meeting the publication costs of this article.

References

1. P. Holtappels, J. Bradley, J. T. S. Irvine, A. Kaiser, and M. Mogensen, *J. Electrochem. Soc.*, **148**, A923 (2001).
2. O. A. Marina, N. L. Canfield, and J. W. Stevenson, *Solid State Ionics*, **149**, 21 (2002).
3. O. A. Marina and L. R. Pederson, in *Proceedings of the 5th European Solid Oxide Fuel Cell Forum*, J. Huijsmans, Editor, p. 481, European SOFC Forum, Lucerne, Switzerland (2002).
4. O. A. Marina and M. Mogensen, *Appl. Catal., A*, **189**, 117 (1999).
5. O. A. Marina, C. Bagger, S. Primdahl, and M. Mogensen, *Solid State Ionics*, **123**, 199 (1999).
6. S. Q. Hui and A. Petric, *J. Electrochem. Soc.*, **149**, J1 (2002).
7. S. Q. Hui and A. Petric, *J. Eur. Ceram. Soc.*, **22**, 1673 (2002).
8. J. Sfeir, P. A. Buffat, P. Möckli, N. Xanthopoulos, R. Vasquez, H. J. Mathieu, J. Van herle, and K. R. Thampi, *J. Catal.*, **202**, 229 (2001).
9. J. Sfeir, J. Van herle, and R. Vasquez, in *Proceedings of the 5th European Solid Oxide Fuel Cell Forum*, J. Huijsmans, Editor, p. 570, European SOFC Forum, Lucerne, Switzerland (2002).
10. S. Primdahl, J. R. Hansen, L. Grahl-Madsen, and P. H. Larsen, *J. Electrochem. Soc.*, **148**, A74 (2001).
11. A.-L. Sauvet and J. Fouletier, *Electrochim. Acta*, **47**, 987 (2001).
12. A.-L. Sauvet and J. T. S. Irvine, in *Proceedings of the 5th European Solid Oxide Fuel Cell Forum*, J. Huijsmans, Editor, p. 490, European SOFC Forum, Lucerne, Switzerland (2002).
13. S. W. Tao and J. T. S. Irvine, *Nat. Mater.*, **2**, 320 (2003).
14. S. W. Tao and J. T. S. Irvine, *J. Electrochem. Soc.*, **151**, A252 (2004).
15. J. J. Bentzen and H. Schwartzbach, *Solid State Ionics*, **40–41**, 942 (1990).
16. N. Q. Minh, *J. Am. Ceram. Soc.*, **76**, 563 (1993).
17. J. Liu, B. D. Madsen, Z. Q. Ji, and S. A. Barnett, *Electrochem. Solid-State Lett.*, **5**, A122 (2002).
18. S. Primdahl and Y. L. Liu, *J. Electrochem. Soc.*, **149**, A1466 (2002).
19. H. Uchida, S. Suzuki, and M. Watanabe, *Electrochem. Solid-State Lett.*, **6**, A174 (2003).
20. J. H. Kuo, H. U. Anderson, and D. M. Sparlin, *J. Solid State Chem.*, **83**, 52 (1989).
21. I. Yasuda and M. Hishinuma, *J. Solid State Chem.*, **123**, 382 (1996).
22. J. Mizusaki, Y. Yonemura, H. Kamata, K. Ohyama, N. Mori, H. Takai, H. Tagawa, M. Dokiya, K. Naraya, T. Sasamoto, H. Inaba, and T. Hashimoto, *Solid State Ionics*, **132**, 167 (2000).
23. M. P. Pechini, U.S. Pat. 3,330,697 (1967).
24. C. Dong, *User's Manual for PowderX*, Institute of Physics, Chinese Academy of Science, Beijing (1998).
25. A. Boultif and D. Louer, *J. Appl. Crystallogr.*, **24**, 987 (1991).
26. J. Mizusaki, H. Tagawa, K. Naraya, and T. Sasamoto, *Solid State Ionics*, **49**, 111 (1991).
27. T. Atsumi and N. Kamegashira, *J. Alloys Compd.*, **257**, 161 (1997).
28. H. Tagawa, J. Mizusaki, Y. Arai, Y. Kuwayama, S. Tsutiya, T. Takeda, and S. Sesido, *Denki Kagaku oyobi Kogyo Butsuri Kagaku*, **58**, 512 (1990).
29. F. A. Kröger and H. J. Vink, in *Solid State Physics*, Vol. 3, F. Seitz and D. Turnbull, Editors, p. 307, Academic Press, New York (1956).
30. R. Moos, A. Gnudi, and K. H. Härdtl, *J. Appl. Phys.*, **78**, 5042 (1995).
31. R. Moos and K. H. Härdtl, *J. Appl. Phys.*, **80**, 393 (1996).
32. R. Moos, S. Schöllhammer, and K. H. Härdtl, *Appl. Phys. A: Mater. Sci. Process.*, **65**, 291 (1997).
33. S. N. Ruddlesden and P. Popper, *Acta Crystallogr.*, **10**, 538 (1957).
34. S. N. Ruddlesden and P. Popper, *Acta Crystallogr.*, **11**, 54 (1958).
35. T. Y. Tien and F. A. Hummel, *Trans. Br. Ceram. Soc.*, **66**, 233 (1967).
36. R. Moos, T. Bischoff, W. Menesklou, and K. H. Härdtl, *J. Mater. Sci.*, **32**, 4247 (1997).
37. R. J. D. Tilley, *J. Solid State Chem.*, **21**, 293 (1977).
38. N. G. Eror and U. Balachandran, *J. Solid State Chem.*, **40**, 85 (1981).
39. U. Balachandran and N. G. Eror, *J. Electrochem. Soc.*, **129**, 1021 (1982).
40. B. F. Flandermeyer, A. K. Agarwal, H. U. Anderson, and M. M. Nasrallah, *J. Mater. Sci.*, **19**, 2593 (1984).
41. S. A. Howard, J. K. Yau, and H. U. Anderson, *J. Appl. Phys.*, **65**, 1492 (1989).
42. M. E. Bowden, D. A. Jefferson, and I. W. M. Brown, *J. Solid State Chem.*, **117**, 88 (1995).
43. J. Canales-Vázquez, M. J. Smith, J. T. S. Irvine, and W. Z. Zhou, *Adv. Funct. Mater.*, **15**, 1000 (2005).
44. H. W. Schmalle, T. Williams, and A. Reller, *Acta Crystallogr., Sect. B: Struct. Sci.*, **B49**, 235 (1993).
45. U. Balachandran and N. G. Eror, *J. Am. Ceram. Soc.*, **64**, C-75 (1981).
46. H. P. R. Frederikse, W. R. Thurber, and W. R. Hosler, *Phys. Rev.*, **134**, A442 (1964).
47. M. Brown, S. Primdahl, and M. Mogensen, *J. Electrochem. Soc.*, **147**, 475 (2000).
48. F. Tietz, G. Stochniol, and A. Naoumidis, in *Proceedings of the 5th European Conference on Advanced Materials and Processes and Applications (Euromat '97)*, Vol. 2, L. A. J. L. Sarton and H. B. Zeedijk, Editors, p. 271, Netherlands Society for Materials Science (1997).
49. F. J. Gardner, M. J. Day, N. P. Brandon, M. N. Pashley, and M. Cassidy, *J. Power Sources*, **86**, 122 (2000).
50. L. Blum, H. P. Buchkremer, S. M. Gross, B. de Haart, J. W. Quadakkers, U. Reisgen, R. Steinberger-Wilckens, R. W. Steinbrech, and F. Tietz, in *Solid Oxide Fuel Cells IX*, S. C. Singhal and J. Mizusaki, Editors, PV 2005–07, p. 39, The Electrochemical Society Proceedings Series, Pennington, NJ (2005).
51. B. A. Boukamp, *Solid State Ionics*, **169**, 65 (2004).
52. S. Primdahl and M. Mogensen, *J. Electrochem. Soc.*, **144**, 3409 (1997).
53. F. T. Ciacchi, K. M. Crane, and S. P. S. Badwal, *Solid State Ionics*, **73**, 49 (1994).
54. N. L. Robertson and J. N. Michaels, *J. Electrochem. Soc.*, **138**, 1494 (1991).
55. P. Holtappels, I. C. Vinke, L. G. J. de Haart, and U. Stimming, *J. Electrochem. Soc.*, **146**, 2976 (1999).
56. J. Jamnik and J. Maier, *J. Electrochem. Soc.*, **146**, 4183 (1999).
57. J. Jamnik and J. Maier, *Phys. Chem. Chem. Phys.*, **3**, 1668 (2001).
58. K. Masuda, A. Kaimai, K. Kawamura, Y. Nigara, T. Kawada, J. Mizusaki, H. Yugami, and H. Arashi, in *Solid Oxide Fuel Cells V*, U. Stimming, S. C. Singhal, H. Tagawa, and W. Lehnert, Editors, PV97–40, p. 473, The Electrochemical Society Proceedings Series, Pennington, NJ (1997).
59. T. Kawada, J. Suzuki, M. Sase, A. Kaimai, K. Yashiro, Y. Nigara, J. Mizusaki, K. Kawamura, and H. Yugami, *J. Electrochem. Soc.*, **149**, E252 (2002).
60. S. Primdahl and M. Mogensen, *J. Electrochem. Soc.*, **145**, 2431 (1998).